Asymmetric transmission through a classical analogue of the Aharonov-Bohm ring

Lei Chen [1,2] Isabella L. Giovannelli [1] Nadav Shaibe [1] and Steven M. Anlage [1,2,*]

[1]*Maryland Quantum Materials Center, Department of Physics, University of Maryland, College Park, Maryland 20742, USA*
[2]*Department of Electrical and Computer Engineering, University of Maryland, College Park, Maryland 20742, USA*

It has been predicted that new physics and technology are enabled for quantum systems that suffer from partial decoherence, in the intermediate range between coherent quantum evolution and incoherent classical physics. We explore the asymmetric transmission through a classical analogue of the Aharonov-Bohm (AB) mesoscopic ring that supports a 3:1 asymmetry in transmission times, augmented with lossy features that act preferentially on the longer-lingering waves. Such a device is realized as a linear microwave graph utilizing a gyrator to create the 3:1 transmission time delay asymmetry, along with both homogeneous and localized losses, to produce an imbalance in wave transmission through the device. We demonstrate asymmetric transmission through the microwave-ring graph as a function of loss in both simulation and experiment, and in both the frequency- and time-domain. The microwave ring-graph results are compared to a numerical simulation representative of a class of recent models proposing dephasing-induced transport asymmetry in few-channel quantum systems, and parallels are noted.

I. INTRODUCTION

There is a deep disparity between the quantum and classical perspectives on physical laws. Our experience with the classical world is dominated by equations of motion that include loss, dissipation, and friction, explicitly breaking time-reversal invariance, and describing phenomena involving large numbers of interacting particles, creating a perception of the "arrow of time" [1,2]. At the microscopic scale we know that the laws of quantum mechanics are time-reversal invariant, and isolated systems are described by unitary time evolution of the quantum state. This poses the question: how do the laws of quantum mechanics segue into those of classical mechanics as one admits stronger interactions with other degrees of freedom? Such questions have been addressed in the fields of fundamental quantum mechanics [3–8], quantum chaos [9], quantum statistical mechanics [1] and thermodynamics [10], and mesoscopic physics [11,12], among others.

A related question is whether or not there is new physics to explore in the regime between pure quantum evolution and classical physics? Can systems described by a mixture of quantum and classical properties show qualitatively new phenomena that are not anticipated by the properties of systems in either limit? More specifically, can a finite degree of quantum "dephasing" be harnessed to perform a new task that is not possible in the fully quantum or fully classical limits? The answers to these questions are relevant to a wide variety of phenomena and applications. For example, coupling a quantum system to additional degrees of freedom can be used for quantum state preparation [13], as a resource for universal quantum computation [14], to simulate open quantum systems [15–17], to enable environment-assisted quantum transport (ENAQT) [18–22], to accomplish fast reset of qubits [23], and for advanced quantum sensing [24]. However, it is interesting to see if other qualitatively new phenomena can be discovered and exploited in this regime.

There has been long-sustained interest in preparing materials and devices that explicitly break time-reversal invariance (TRI) to create nonreciprocal transport for electrons between equivalent contacts [11,12], for example. Many proposals to create nonreciprocal transport are inspired by Maxwell demons [25,26], thermally driven ratchets [27], noncentrosymmetric materials [28], and efforts to violate detailed balance in thermal radiation [29,30]. Systems with nonlinearity have been utilized to demonstrate asymmetric transport [31,32]. One approach to selectively transferring electrons is to create wave-function interferometers that preferentially pass matter waves moving in one direction but not the other, and such devices require breaking of time-reversal invariance [33,34]. In particular, the Aharonov-Bohm matter-wave interferometer, augmented with decoherence to induce nonreciprocity [35], has been proposed as one possible setting for this type of device.

The Aharonov–Bohm (AB) effect is a quantum mechanical phenomenon in which an electrically charged particle of charge q is affected by an electromagnetic potential (through the vector potential $\vec{A}$) in the absence of a magnetic or electric field at the location of the particle [36]. This effect gives rise to a type of "action at a distance" in which a particle can be affected by electromagnetic fields even if it does not experience them directly. The traditional setting for the AB effect is a finite region of space containing nonzero magnetic flux Φ surrounded by a field-free region. A beam of charged particles is sent through the field-free region in a ring geometry that fully incorporates the region of finite flux within the ring. The charges show interferometric properties arising from a
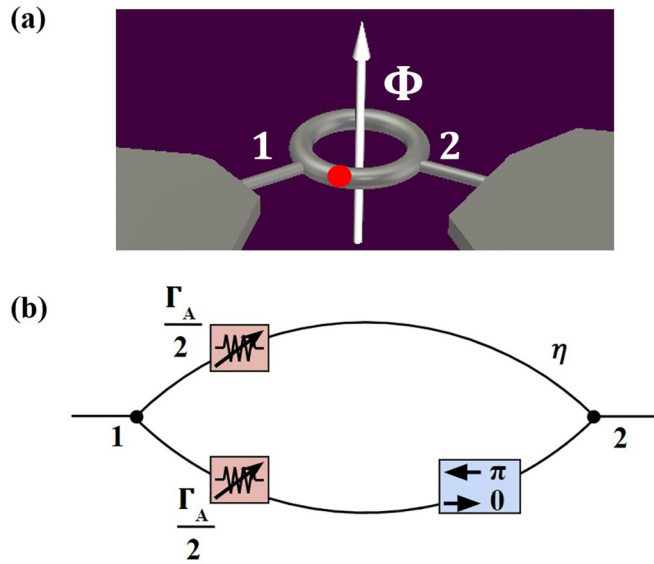
(a)

(b)

FIG. 1. Schematic layout of an Aharonov–Bohm ring and a corresponding classical microwave graph analogue. Panel (a) shows the device layout of a two-port Aharonov–Bohm ring made of clean metal. The penetrating magnetic flux Φ creates nonreciprocal transmission times for electron wave packets transiting the ring. The red dot marks an inelastic scattering center. Panel (b) shows the classical analogue microwave graph realization. A microwave gyrator (see Fig. 9) creates the π phase difference for waves traveling in opposite directions on the lower bond. The variable attenuators of strength $\Gamma_A/2$ act as a localized loss center. Panel (a) after Ref. [38].

quantum phase shift $e^{\frac{iq}{\hbar} \int \vec{A} \cdot d\vec{\ell}}$ upon traversing each branch of the ring. Upon recombination, parts of the wave packet that pass through different branches of the ring create interference that depends on Φ/Φ_0, where $\Phi_0 = h/q$ is the flux quantum for the charges, and h is Planck's constant.

In Refs. [33,34,37,38], the authors consider an Aharonov-Bohm (AB) ring in a mesoscopic conducting sample that suffers from a certain degree of "dephasing" in electron transport. Specifically, they consider a single-channel, two-terminal AB ring enclosing a DC magnetic flux (as described above). Figure 1(a) shows the schematic of the proposed mesoscopic Aharonov–Bohm ring. This device has two key features that are proposed to bring about new behavior. First, this device has nonreciprocal transmission times as a result of the direction-dependent phase shift that the electron picks up as it traverses the ring. An electron wave packet propagating through the device from left to right, say, will split into two parts at the left combiner. Along each of these paths, the respective wave will accumulate a phase. For the waves to constructively recombine at the other end, they must be in phase with each other, hence the net phase difference accumulated must be $2\pi n, n \in \mathbb{Z}$. The phase difference accumulated as the electron traverses the ring is given by [34] $\Delta\phi = k\Delta l \pm 2\pi \frac{\Phi}{\Phi_0}$ where Δl is the difference in length between the two arms and k is the wave number of the electron. In Ref. [34], the author considers the case where $k\Delta l = \frac{\pi}{2}$ and $2\pi \frac{\Phi}{\Phi_0} = \frac{\pi}{2}$, leading to $\Delta\phi_{1\rightarrow2} = 0$ and $\Delta\phi_{2\rightarrow1} = \pi$. Thus, electrons traveling from port 1 to port 2 would suffer no relative phase shift and immediately exit the ring. However,

electrons traveling from port 2 to port 1 will suffer destructive interference, due to the π phase difference, causing the wave packet to reflect back around the ring. Hence an electron starting at port 2 will need to traverse the ring three times to accumulate a net phase difference of $2\pi n, n \in \mathbb{Z}$, allowing it to coherently recombine and exit the ring. This consequently leads to a nonreciprocal 3-to-1 ratio of transmission times, as further discussed in Ref. [38].

The second key feature arises when a finite degree of quantum dephasing is added in the form of a defect or "deep trap" in the semiconducting ring [12,35,37], denoted as the red dot in Fig. 1(a). This defect works as a "dephasing site" by taking a passing electron wave packet out of the conduction band with some probability. When an electron is captured, the state is projected onto an eigenstate of the trap and it loses all memory of its prior state, including its phase and the direction that it was traveling. The electron is eventually released back into the conduction band with equal probability of traveling to the left or right. A more detailed description of this process is given in Ref. [12]. It is argued in Refs. [12,38] that this dephasing site, combined with the engineered 3-to-1 transmission time ratio, leads to a net asymmetry in transmission probability. The argument is that since electrons traveling from port 2 to port 1 need to make three times as many passes as electrons traveling from port 1 to port 2, they then have three times as many chances of interacting with the dephasing site. Hence, electrons traveling in that direction have a lower chance of being transmitted. Supporting simulation results are discussed in Ref. [12] where they show that not only is this asymmetry in transmission probability present, but it has a nonmonotonic dependence on the modelled dephasing rate.

In addition to the explicit proposals made in Refs. [33,37,38], a few other works have hinted at this asymmetric transmission probability effect. The work of Entin-Wohlman *et al.* essentially considers a quantum ring subjected to an external magnetic field and suffering partial dephasing in electron transport around the graph. They calculate that this results in a loss of detailed balance in equilibrium, and the creation of a net current between two points in the ring [39]. A cold atom version of a *dissipative* AB-ring in momentum space, roughly similar to the quantum models cited above [12,35,37], has demonstrated nonreciprocal quantum transport [40]. This approach utilizes a synthetic magnetic flux and laser-induced *loss of atoms* in a Bose-Einstein condensate to break inversion and time-reversal symmetries, and demonstrates directional atom flow.

In this paper, our objective is to examine the properties of a *classical analogue* of the mesoscopic AB-ring proposed in Refs. [33,37,38]. In particular, we are motivated by their proposition that quantum wave interference, combined with finite dephasing can lead to asymmetric transmission. Our goal is to see if parallel behavior can be observed in a purely classical setting. Specifically, we want to understand if classical wave interference effects, combined with dissipation, give rise to asymmetric wave propagation.

The outline of the paper is as follows. We begin by discussing the background for the experiment, where we provide a brief overview of the parasitic channel phenomenology that provides an organizing principle for understanding the effects of loss on our experimental results. We then present

simulations of the microwave-ring graph and demonstrate the properties required to achieve asymmetric transmission. A number of complications are added to the simulations to represent the experimental situation, and the key properties are shown to survive. Next we present the experimental realization of the microwave ring-graph, and discuss measurements of the scattering matrix and time delays in both the frequency and time domains, and find good consistency with the simulations. Finally we present results on the transmission asymmetry through the graph in experiment, and compare to expectations based on simulations.

II. BACKGROUND

There is a long history of using microwave circuits and resonant microwave billiards to emulate the wave interference properties of quantum systems [41,42]. Quantum billiards are simulated using microwave resonators, where the analogy between the Schrödinger equation for the wave function ψ and the electromagnetic Helmholtz equation for one component of electric field $\vec{E}$ is particularly clear in two-dimensions [43–52]. For example, it was shown that there is an analogy between the Poynting vector for energy flow in the quasi-two-dimensional electromagnetic cavity and the probability current in the corresponding quantum system [53]. Similarly, the analogy between solutions to the Schrodinger equation on multiconnected molecules [54] and the wave equation on networks of microwave graphs has been noted [55].

In this paper we will be adopting the Heidelberg picture of wave scattering [56–64] to describe scattering in non-Hermitian systems. A Hamiltonian $\mathcal{H}_0$ with real eigenvalues describes the closed system in the absence of losses. We include N eigenmodes of $\mathcal{H}_0$ in the scattering description of the system. The localized losses are treated as L absorbing channels, and the couplings of the N modes to the L absorbing channels are collected in a matrix A [65]. One can define an associated matrix $\Gamma_A = AA^\dagger$ of dimension $N \times N$ that evaluates the overlap of the N resonant eigenmodes of the closed system at the location of loss in the system. The $M \times M$ scattering matrix between the M observable channels is given by $S(E) = \frac{1_M - iK_A}{1_M + iK_A}$, where the Wigner reaction matrix K_A (related to electromagnetic impedance [60,66–70]) is given by $K_A = \pi W^\dagger \frac{1}{E - \mathcal{H}_{\text{eff}}} W$ [60,66,71]. Here W is the $N \times M$ matrix of couplings of the N eigenmodes to the M scattering channels, and $\mathcal{H}_{\text{eff}} = \mathcal{H}_0 - i\Gamma_A$ is the non-Hermitian ($\mathcal{H}_{\text{eff}}^\dagger \neq \mathcal{H}_{\text{eff}}$) effective Hamiltonian of the lossy system. Note that the scattering matrix $S(E)$ is the upper left block of a larger $(M + L) \times (M + L)$-dimensional *Hermitian* scattering matrix $\mathcal{S}(E)$ that describes both the observable and hidden (lossy or parasitic) scattering channels (we assume that $M + L \ll N$) [65]. As such, the $M \times M$ scattering matrix $S(E)$ is subunitary because some of the flux injected through the M observable scattering channels is lost to the L hidden parasitic channels. In addition, one can model uniform attenuation η on the scattering matrix by evaluating the energy (or equivalently frequency of the microwaves) with an imaginary offset $E \rightarrow E + i\eta$, as $S(E + i\eta)$.

We note that the Heidelberg picture is a simple phenomenological approach to describing loss (both lumped and uniform) that is quite generic, and therefore applies to all

sorts of classical wave scattering systems (electromagnetic, acoustic, mechanical, etc.). However, it is not a microscopic theory, and in the case of quantum systems suffering from decoherence, it altogether fails to capture the quantum degrees of freedom, and their associated quantum interactions with the scattering system. As such, the Heidelberg picture has no microscopic justification in describing the scattering properties of quantum systems suffering from decoherence.

In Ref. [72] it was experimentally demonstrated that the statistical properties of the scattering matrix of a microwave cavity with variable uniform loss were described by a simple dephasing-lead model borrowed from a treatment that utilized the parasitic channel (Heidelberg) model of dephasing in mesoscopic transport [73–75]. The uniform attenuation of the quasi two-dimensional microwave cavity (parameterized as the dimensionless quantity $\alpha = k^2 A / 4\pi Q$, where $k = \omega/c$, ω is angular frequency, A is the area of the billiard, and Q is the typical quality factor of the resonant modes) was found to be directly proportional to the dimensionless phenomenological dephasing rate γ that governs the statistics of the scattering (S) matrix and conductance in the corresponding mesoscopic billiard [74,75], as $\gamma = 4\pi\alpha$ over a wide range of microwave loss. (It can be shown that α is related to the uniform attenuation as $\alpha = \frac{\eta}{2\Delta}$, where Δ is the mean spacing between modes of the closed system described by $\mathcal{H}_0$ [72,76].) This work demonstrated that the statistical fluctuations of the wave interference properties of both the classical microwave experiment, and the model quantum system, have the same dependence on a single parameter. We refer to this single-parameter dependence of the scattering matrix statistical properties as the "parasitic channel phenomenology" (PCP). We shall explore the PCP further in this paper through a study of wave interference effects in a classical analogue of the AB-ring graph.

Here we consider quasi-one-dimensional microwave network analogues of quantum graphs that emulate corresponding few-channel mesoscopic conducting quantum systems. Quantum graphs are one-dimensional metric graphs with complex topology that support excitations described by the Schrödinger operator [77,78] that can be used to describe quantum transport through a variety of structures, including molecules [54,79], quantum wires [80,81], disordered two-dimensional quantum dots [81–83], etc. In general, microwave graphs consist of vertices connected by bonds, and we consider the propagation of microwave signals on the bonds and the resulting interference that occurs when multiple bonds meet at a vertex. Microwave graphs have been used to investigate many aspects of wave scattering theory, including statistics of the Wigner reaction matrix (analogous to electromagnetic impedance) [55], topological edge invariants [84], deviations from the predictions of random matrix theory [85], etc. The PCP has also be used to quantify the effects of dissipation on the scattering matrix statistics of microwave graphs [68,86].

We introduce a linear two-terminal, single-channel microwave graph to emulate the wave interference properties of a mesoscopic Aharonov–Bohm ring, and study its scattering properties in both the frequency domain and the time domain. In particular, our objective is to demonstrate asymmetric transmission by utilizing a specific combination of
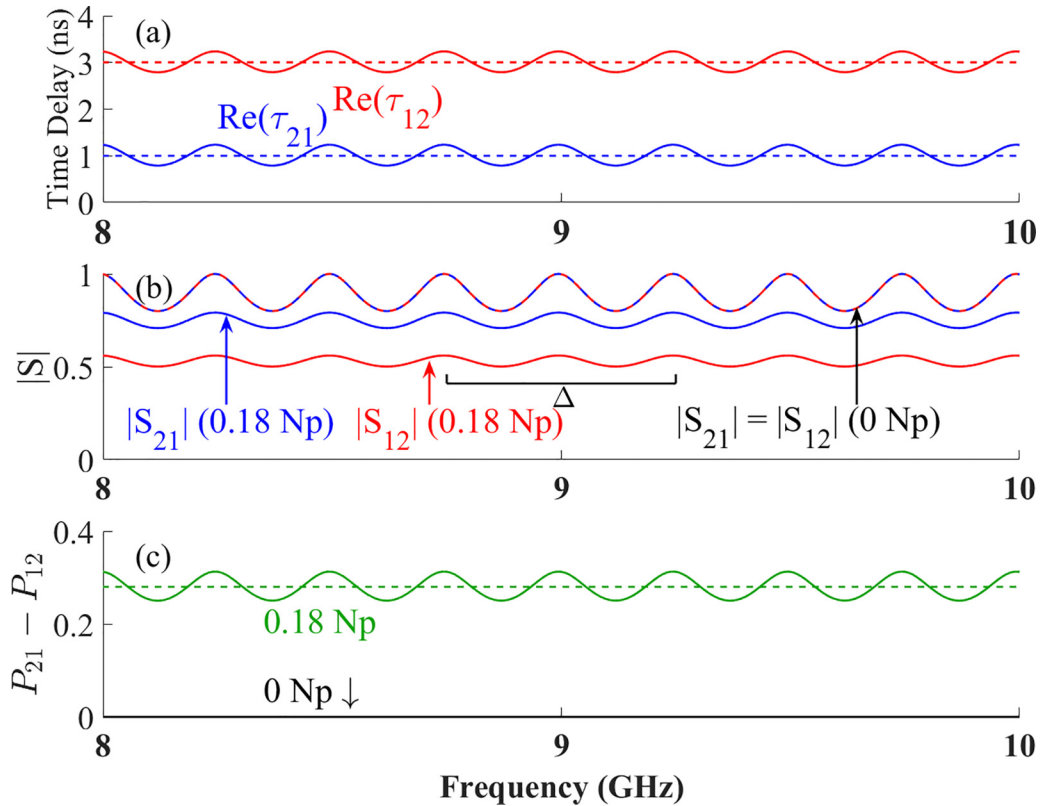
FIG. 2. Simulated properties of the microwave AB-ring graph with uniform attenuation $\eta = 0$. (a) Real part of transmission time delays of the Aharonov-Bohm microwave ring graph simulation for the case of localized attenuation $\Gamma_A/2 = 0.18$ Np. Blue curve shows $\text{Re}[\tau_{21}]$ and red curve shows $\text{Re}[\tau_{12}]$, and the dashed lines show the mean values, demonstrating a 3:1 ratio. (b) Linear transmission magnitudes in both directions for the case of $\Gamma_A/2 = 0$ Np attenuation and $\Gamma_A/2 = 0.18$ Np local attenuation. Blue corresponds to $|S_{21}|$ while red corresponds to $|S_{12}|$. With no attenuation the transmission magnitudes are identical. The scale bar gives the expected periodicity frequency scale ($\Delta = 0.5$ GHz) for the shape resonances of a simple ring graph. (c) The asymmetric transmission $P_{21} - P_{12}$ as a function of frequency for the case of $\Gamma_A/2 = 0.18$ Np local attenuation.

wave interference and attenuation. The microwave graph in Fig. 1(b) satisfies all of the conditions for displaying asymmetric transmission, including broken time-reversal invariance, a subunitary scattering matrix, and a gyrator which produces a broadband constant π-phase shift for waves going in one direction [37]. We note that the gyrator effectively performs the function of a Faraday rotator, as originally utilized by Rayleigh to create nonreciprocal transmission of light [12,87,88]. We demonstrate that the real part of forward and backward transmission time delays have a 3:1 ratio in a broad range of frequency, which establishes the first condition for asymmetric transmission. We also introduce a localized loss Γ_A (exploiting the PCP to phenomenologically treat dissipation [72]) in the ring graph, and adjust the left/right transmission coefficients by varying the attenuation $\Gamma_A/2$ of two objects, in a balanced manner. We demonstrate the dependence of asymmetric transmission on the loss rate through the attenuation variation.

III. SIMULATIONS

We first simulate the nonreciprocal transmission effect of the microwave ring-graph in CST Microwave Studio. In particular we use a circuit modeling package to create a faithful model of the microwave graph (see Appendix A and Fig. S1 in

the Supplemental Material [89]). We implement the complete circuit shown in Fig. 1(b) with equal electrical lengths (i.e., propagation phase shifts) for the upper and lower bonds. In the remainder of the paper we utilize the formalism of Sec. II treating energy and frequency of the microwaves as equivalent quantities.

A. Frequency domain simulations

The complex transmission time delays (see Appendix C) for both directions (S_{21} and S_{12}) can be calculated from the complex scattering matrix data as $\tau_T^{12,21} = -i\frac{d}{df}\log(S_{12,21})$ [34,90–95]. Figure 2(a) shows the simulation comparison between the real part of the transmission time delay for the two directions, demonstrating the required 3:1 ratio, modulo small oscillations associated with the shape resonances of the microwave graph [95]. Figure 2(b) shows the transmission magnitudes $|S_{12}|$ and $|S_{21}|$ through the microwave graph under several different attenuation settings. When the lumped attenuation $\Gamma_A/2$ is 0 Nepers and there are no uniform losses, i.e., no loss in the entire system and a unitary S-matrix, the two transmission paths have identical transmission magnitude as a function of frequency. As the lumped attenuation increases, significant differences begin to show up between the two transmission amplitudes.
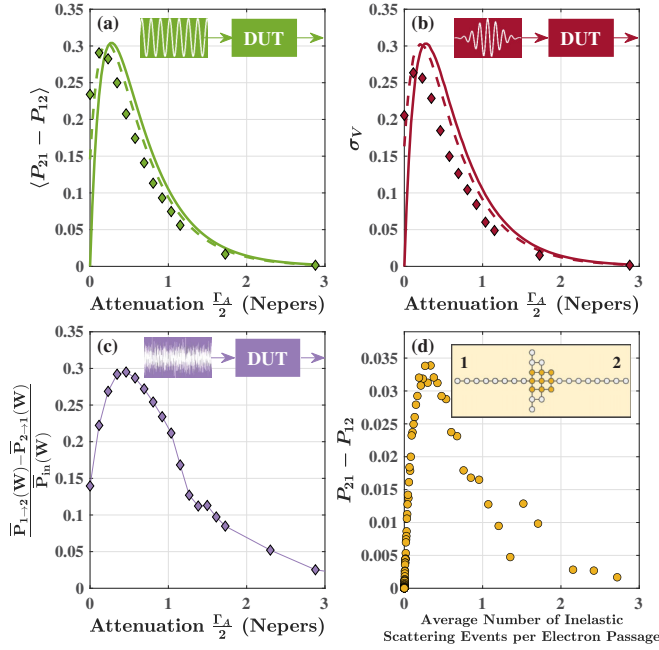
FIG. 3. Asymmetric transmission through microwave AB-ring graph and a model mesoscopic electron device. (a) Summary of the frequency domain results. In the upper right is a schematic of how these measurements work. For frequency domain measurements, a wave with a single frequency is sent through the device, this is done multiple times over a frequency range. For all curves, the quantity $P_{21} - P_{12}$ is averaged over the frequency range 8.25–8.75 GHz, which is denoted as $\langle P_{21} - P_{12} \rangle$. The solid line is from simulation where only the localized attenuation from the attenuators is considered. The dashed line is also from the same simulation but with finite uniform attenuation added. The discrete diamond points are from experimental data. (b) Summary of the time domain results expressed in terms of $\sigma_V = (|V_{21}|^2 - |V_{12}|^2)/|V_{in}|^2$. For these time domain measurements, a 1 ns wide Gaussian pulse with a carrier frequency of 8.5 GHz is sent into the device. The legend has the same meaning as in panel (a). (c) Noise source input experimental results. This data was taken in the frequency domain with a microwave noise source input as a function of total attenuation in the graph. It is plotted as frequency-averaged transmitted power difference, normalized by the measured incident power, $(\bar{P}_{21} - \bar{P}_{12})/\bar{P}_{in}$. (d) Tight-binding model of triangle-shaped mesoscopic device with a dephasing center, as a function of the average number of inelastic scattering events per electron passage through the structure. From Refs. [12,35]. Data provided courtesy of Dr. Jochen Mannhart, Max Planck Institute for Solid State Research, Stuttgart, Germany.

The asymmetric transmission behavior of the ring graph at each frequency can be quantified as the transmission probability difference: $P_{21} - P_{12} = |S_{21}|^2 - |S_{12}|^2$. Note that $P_{21} - P_{12}$ is bounded between 0 and 1, and is frequency-dependent in general. If there is no asymmetric transmission then $P_{21} - P_{12} = 0$, while a nonzero value implies some degree of asymmetric transmission. Figure 2(c) shows $P_{21} - P_{12}$ as a function of frequency for the $\Gamma_A/2 = 0.18$ Np attenuation case, revealing a frequency-averaged value (dashed green line) of $\langle P_{21} - P_{12} \rangle = 0.28$.

To explore the asymmetric transmission further, Fig. 3(a) shows $P_{21} - P_{12}$ as a function of lumped attenuation on each

bond ($\Gamma_A/2$) for the model graph. Due to the periodic wiggles arising from the shape resonances of the ring graph, we perform an average of $P_{21} - P_{12}$ over the range of frequencies 8.25–8.75 GHz corresponding to one period of the shape resonances ($\Delta = 0.5$ GHz), and designate it as $\langle P_{21} - P_{12} \rangle$. The frequency averaged transmission asymmetry $\langle P_{21} - P_{12} \rangle$ shows a nonmonotonic bell shaped behavior as the lumped attenuation increases.

We have also simulated the more realistic case where both uniform attenuation and lumped variable attenuation are present in the AB-ring microwave graph. We set the parameters of the simulated coaxial cables to approximately match those used in the experiments discussed below, leading to a frequency-dependent uniform attenuation η described by Eq. S1 in the Supplemental Material [89]. The resulting transmission asymmetry $\langle P_{21} - P_{12} \rangle$ versus lumped attenuation is also shown in Fig. 3(a) as a dashed line. The main difference is that uniform attenuation effectively establishes a finite amount of asymmetric transmission even with zero lumped attenuation.

B. Time domain simulations

Time-domain simulations have been performed with the model microwave ring-graph shown in Fig. S1 (see Appendix A and Supplemental Material [89] section "Simulations"). Gaussian wave packets with 1 ns width and a chosen carrier frequency are injected into the graph from each port. The output pulses show the expected 3:1 asymmetry in time delay upon going through the graph, as shown in Fig. S2 in Ref. [89]. To quantify the transmission probability difference in the time-domain, we form the quantity $\sigma_V = (|V_{21}|^2 - |V_{12}|^2)/|V_{in}|^2$, where V_{21} and V_{12} are the voltage amplitudes of the transmitted pulses in the simulations and V_{in} is the amplitude of the incident pulse. Figure 3(b) shows σ_V as a function of the lumped attenuation (solid line). As the lumped attenuation increases the transmitted wave packets first show an increasingly asymmetric transmission probability. However, beyond about $\Gamma_A/2 = 0.29$ Np the wave packets show reduced transmission asymmetry. The addition of uniform loss serves to shift the σ_V curve (dashed line), just as with the frequency domain simulations in Fig. 3(a).

These simulation results of the microwave ring-graph in both the frequency- and time-domains establish the basic properties of asymmetric transmission.

IV. EXPERIMENT

The microwave graph consists of a coaxial cable structure that supports a single mode of propagation for microwave frequencies below the cutoff of higher-order modes, which is well beyond our operating frequency range [55]. An Aharonov–Bohm ring uses magnetic flux to produce nonreciprocal transmission times in a simple electron interferometer. To mimic that effect, we use a microwave gyrator [96–98] to create a unidirectional π phase shift in a microwave ring network. As illustrated in Figs. 9 and S3 [89] this is achieved by means of two microwave circulators that are configured with short and open circuits on their third ports to create the requisite π relative phase shift. We also demonstrate in
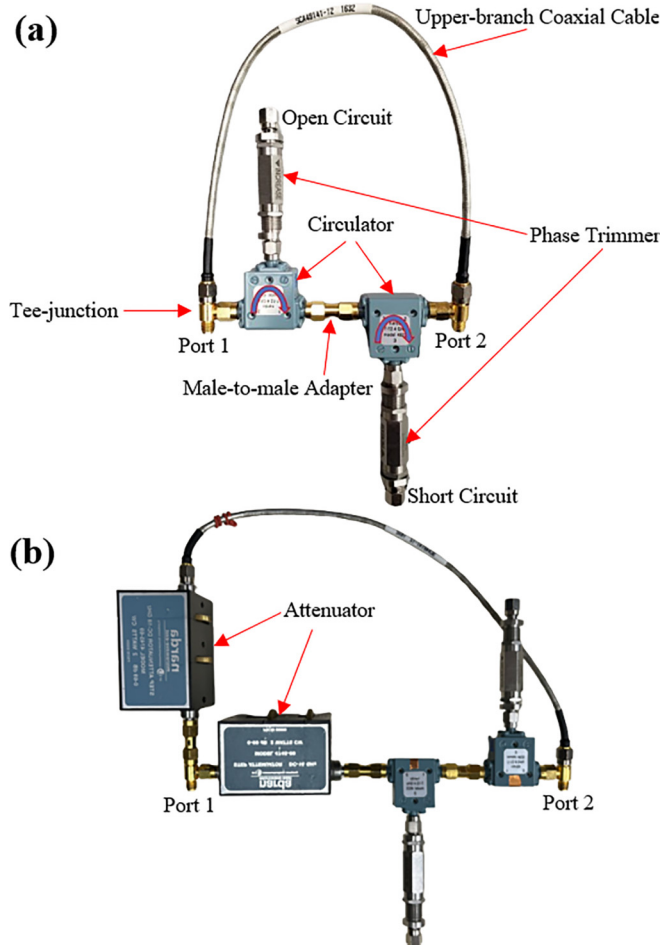
FIG. 4. (a) Photograph of the Aharonov–Bohm microwave ring graph constructed with the gyrator from Fig. 9. The upper branch is a single coaxial cable matching the electrical length of the lower branch. This is the experimental realization of the schematic shown in Fig. 1(b), without the attenuators. (b) Microwave graph analogue Aharonov-Bohm ring for the two-attenuator case, with one attenuator of strength $\Gamma_A/2$ on each bond.

Appendix B that this relative phase difference is approximately achieved over a broad frequency range (7–12.4 GHz) with virtually no difference in attenuation of the signals in the two directions.

Next, we construct the Aharonov–Bohm analogue ring microwave graph (see Fig. 4) using the gyrator design. The key is to add an upper branch to the ring that has the same electrical length as the gyrator, so that waves traveling from left to right in both branches would go through the same electrical length. Equating the electrical lengths of the branches also has the effect of eliminating the Feshbach modes, leaving only the shape resonances of the ring graph (see Refs. [95] and [99]). We measured the electrical length of the gyrator and a series of single coaxial cables, and selected a 12-inch-long coaxial cable as the upper branch. We then perform some fine-tuning on both phase trimmers to achieve an electrical length on the lower bond as close as possible to that of the 12-inch cable. The 12-inch coaxial cable has an electrical length of 0.4386 m, and we manage to adjust the electrical length of the gyrator to be 0.4385 m while maintaining a near π phase difference

for left/right transmission. The resulting microwave analogue of the AB graph with π flux-induced phase shift is shown in Fig. 4(a) (no lumped loss) and Fig. 4(b) (including lumped loss Γ_A).

The losses in the microwave graph arise from two sources. There exists roughly uniform attenuation of the microwave signals associated with the insertion loss of the coaxial cables, circulators, phase trimmers, microwave tees, adapters, and terminations. The attenuation η of the coaxial cables used here, which dominates the uniform attenuation in the circuit, has been characterized in Appendix B of Ref. [95]. The second source of loss is associated with the variable lumped (localized absorbing channels) attenuators Γ_A, shown schematically in Fig. 1(b). In the experiments both types of loss in the microwave graph will be considered. Note that in all comparisons of microwave data and mesoscopic theory we treat the independent variables frequency f and energy E as interchangeable.

A. Frequency domain measurements

We measure the scattering (S) matrix of the two-port microwave ring-graph as a function of frequency. A Keysight N5242B network analyzer (PNA-X) is calibrated with a Keysight N4691D Electronic Calibration kit over the 7 to 12.4 GHz frequency range with a frequency step size of 168 750 Hz. An Agilent Technologies N5242A vector network analyzer (VNA) is also used over the same frequency range; it is calibrated with an Agilent N4691-60001 Electronic Calibration kit with the same frequency step size. The device under test (DUT) is attached at the calibration planes of the network analyzer and the 2×2 S-matrix is measured as a function of frequency for various settings of the lumped attenuators in the microwave ring-graph.

To measure the response of the microwave ring-graph to incoherent input signals, a Microwave Semiconductor Corp (MSC) MC65242, 1.0 to 18 GHz noise source producing output excess noise ratio (ENR) of 31.5 dB, is used to create broadband noise in the microwave domain. The noise signal is amplified by two mini-circuits amplifiers (ZX60-183A-S+) each with a bandwidth of 6 to 18 GHz. The two amplifiers are separated by one Narda-MITEQ (94S46) attenuator with a bandwidth of 4 to 18 GHz. The amplified noise source is connected to one port of the microwave ring-graph while the other port of the graph is connected to a network analyzer (Keysight N5242B). The network analyzer is used in receiving mode, with a resolution bandwidth of 10 kHz and 200 point averaging, to measure the transmitted power in a frequency resolved manner. The experiment is repeated with the ports on the microwave ring-graph reversed.

B. Time domain measurements

The broadband nature of the 3:1 transmission time ratio of our AB-ring graph analogue allows us to utilize widebandwidth pulses to investigate the asymmetric transmission through the device. We perform pulse propagation measurements through the microwave ring-graph in both directions, systematically varying the center frequency of the pulse, and measuring the time delays and amplitudes of the transmitted
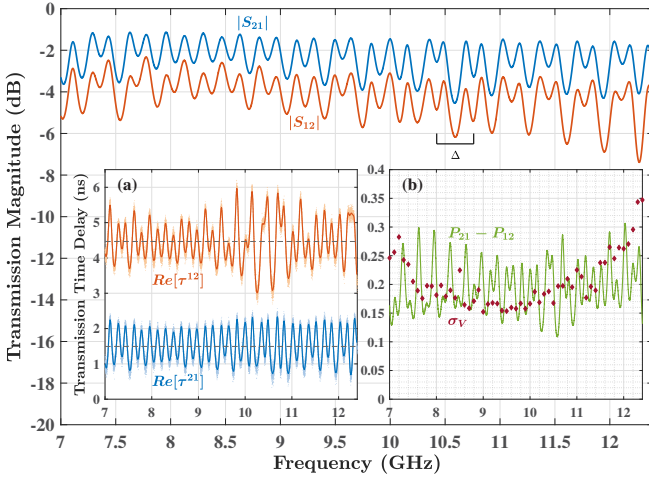
FIG. 5. Measured S-matrix transmission data for the microwave ring-graph in Fig. 4(a) with approximately uniform attenuation, as a function of frequency. The scale bar gives the expected periodicity frequency scale ($\Delta = 0.342$ GHz) for the shape resonances of a simple ring graph. Note that $|S_{21}|$ is larger than the $|S_{12}|$ consistently across the full frequency range. Inset (a) shows the real part of the transmission time delays of the graph. We see that $\mathrm{Re}[\tau_T^{12}] \approx 3 \times \mathrm{Re}[\tau_T^{21}]$ over the full frequency range. The dashed lines represent the average of the time delays. Inset (b) shows transmission probability asymmetry of the graph measured in both the frequency domain ($P_{21} - P_{12}$, green line) and time domain (σ_V, red diamonds) as a function of frequency.

pulses. A Tektronix model AWG70001B Arbitrary Waveform Generator (AWG) is attached to the input port of the DUT, and the other port is attached to a Keysight/Infiniium model UXR0104A real-time oscilloscope. The input pulse created by the AWG is designed to be a 1-ns long Gaussian modulated pulse of center frequency f_c, with f_c ranging in value from 7 to 12.4 GHz. The pulse is measured by connecting the output of the AWG directly to the oscilloscope to establish the amplitude and timing of the incident pulse. The measurement is then repeated with the microwave ring-graph present in the other orientation.

We note that prior measurements of pulse transport in microwave graphs has focused on the delay distribution and identifying orbits due to short closed loops in the graph [100].

C. Frequency-domain experimental results

We measure the 2×2 scattering (S)-matrix of the Aharonov-Bohm ring microwave graph shown in Fig. 4(a) (with approximately uniform attenuation only) from 7 to 12.4 GHz, and plot the results in Fig. 5. The periodic wiggles in the plot come from the shape resonances of the graph, which have been thoroughly studied in Refs. [95] and [99], and discussed for the simulations. The periodicity of the shape resonances depends on the total circumferential length of the graph $\Sigma = 0.8771$ m, which corresponds to a repetition frequency of $\Delta = \frac{c}{\Sigma} = 0.342$ GHz. Note that waves propagating anticlockwise around the microwave ring satisfy the ordinary shape resonance conditions, $f_n = \frac{c}{\Sigma} n$, with $n = 1, 2, 3, \ldots$. However, waves traveling clockwise around the microwave ring suffer an additional π phase shift upon passage through

the gyrator, resulting in a different resonance condition, $f_m = \frac{c}{\Sigma}(m - \frac{1}{2})$, with $m = 1, 2, 3, \ldots$, creating a series of modes that begin at $\Delta/2 = 0.171$ GHz, and then alternate with the anticlockwise modes as a function of frequency, consistent with the periodicity shown in Fig. 5. This creates two distinct sets of S-matrix poles and zeros for the modes of the microwave ring-graph (see Supplemental Material [89] section "Poles and Zeros of the S-Matrix of the Microwave Ring-Graph").

D. Transmission time delays

The measured results for the real part of transmission time delay in both directions, $\mathrm{Re}[\tau_T^{21}]$, $\mathrm{Re}[\tau_T^{12}]$, are shown in Fig. 5(a). The mean values are clearly different, while the regular variations of the transmission time delay plot come from the shape resonances of the ring graph, although here we are more interested in the ratio between the two transmission time delays. The mean values are $\langle \mathrm{Re}[\tau_T^{21}] \rangle = 1.49$ ns and $\langle \mathrm{Re}[\tau_T^{12}] \rangle = 4.47$ ns, with a ratio of 2.99. This demonstrates the average 3:1 ratio for the two transmission time delays in the Aharonov–Bohm ring microwave graph, based on frequency-domain data.

E. Asymmetric transmission

Figure 5 shows a comparison between forward and reverse transmission amplitudes $|S_{21}|$ and $|S_{12}|$ in the microwave ring-graph, where it can be seen that $|S_{21}| > |S_{12}|$ for all frequencies in the bandwidth of the device. The asymmetric transmission probability $P_{21} - P_{12}$ is plotted as a function of frequency in Fig. 5(b) (green line), demonstrating the broadband nature of the effect.

In addition to measuring the microwave ring-graph with coherent sources in the frequency domain and time domain, we are curious to see how it behaves when subjected to a broadband noise source. It is interesting to see whether or not the asymmetric transmission properties are also exhibited when the AB-ring graph is excited by incoherent noise. Figure 6 shows the results of such an experiment, in which a microwave noise source is used to illuminate one port of the graph. In this case the transmitted signal is measured in a frequency-resolved manner by a network analyzer operating in receiver mode, as discussed in Sec. IV A. The experiment demonstrates broadband asymmetric transmission over the bandwidth of the device. The bandwidth-averaged asymmetric transmission probability was measured as a function of total attenuation in the microwave ring-graph [Fig. 4(b)], and the results are shown in Fig. 3(c). This result shows that the nonmonotonic dependence of transmission asymmetry exists even for a completely incoherent source of microwaves.

F. Time-domain experiments

The results presented so far have been obtained from microwave scattering matrix measurements performed entirely in the frequency domain. Electrons in mesoscopic systems are modeled as quantum wave packets in the time domain. Electron wave packets do not have a single energy, as implied by our time-delay results obtain from S-matrix data, presented above. After demonstrating a 3:1 ratio between
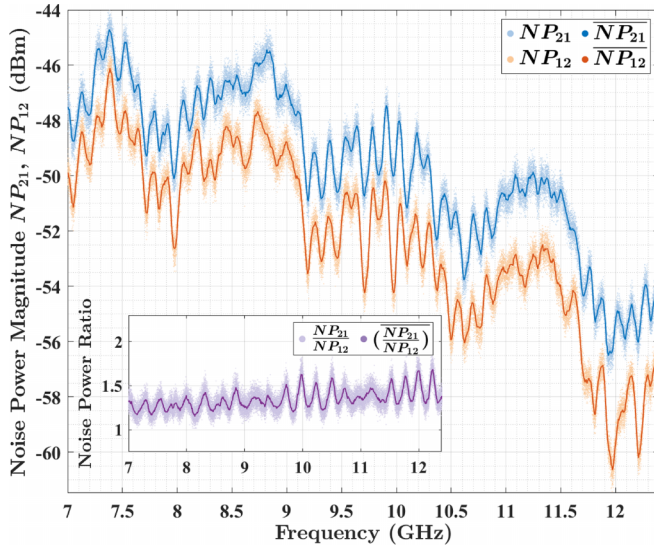
FIG. 6. Measurements of asymmetric noise power transmission (NP_{12} and NP_{21} in units of dBm) as a function of frequency through the AB-microwave graph having only uniform attenuation, when subjected to a broadband noise source. Averaging ($\overline{NP}_{12}$, $\overline{NP}_{21}$) is performed by sectioning the data in groups of 50 frequency points and replacing each of these groups with their respective mean value. Inset shows the asymmetric transmission power ratio $\frac{NP_{21}}{NP_{12}}$ in linear scale over the bandwidth of the graph, showing a mean value of 1.35. Averaging for $\left(\frac{NP_{21}}{NP_{12}}\right)$ is performed in the same way as described above for $\overline{NP}_{12}$ and $\overline{NP}_{21}$.

the two transmission time delays from the frequency-domain data, the question arises whether or not we can demonstrate the asymmetric delay directly in the time domain.

Figure 7 shows representative time-domain results of transmitted pulses emerging at each port when sending in the pulse from the other port. Here, an arbitrary waveform generator (AWG) generates the gaussian-modulated pulse of fixed carrier frequency f_c used in the time-domain measurements. The pulse is a 1-ns wide Gaussian amplitude modulation of an $f_c = 8.5$ GHz carrier signal. Such a pulse includes approximately 1 GHz bandwidth, which is well within the operating bandwidth of our gyrator-based microwave ring-graph. The pulse will have the effect of averaging the nonreciprocal properties of the graph over a finite bandwidth. Here DUT is the device under test (the microwave ring-graph), and the oscilloscope records the incident and transmitted signals. We measured the pulse transmission in both directions, and plot them on the same time axis. Shown for reference (yellow pulse in Fig. 7) is the incident pulse on the DUT, illustrating the relatively modest effects of pulse dispersion in the experiment. Figure 7 demonstrates directly a 3:1 ratio of the transmission time delays for pulses propagating through the AB graph in opposite directions. From the plot, the transmitted pulse from port 2 to port 1, V_{12}, has smaller amplitude compared to the transmitted pulse from port 1 to port 2, V_{21}.

The red diamonds in Fig. 5(b) show the pulse transmission asymmetry parameter $\sigma_V = (|V_{21}|^2 - |V_{12}|^2)/|V_{in}|^2$ versus pulse center frequency from the measured time-domain results in Fig. S4 of Ref. [89]. The results are in good agreement with the transmission probability asymmetry from
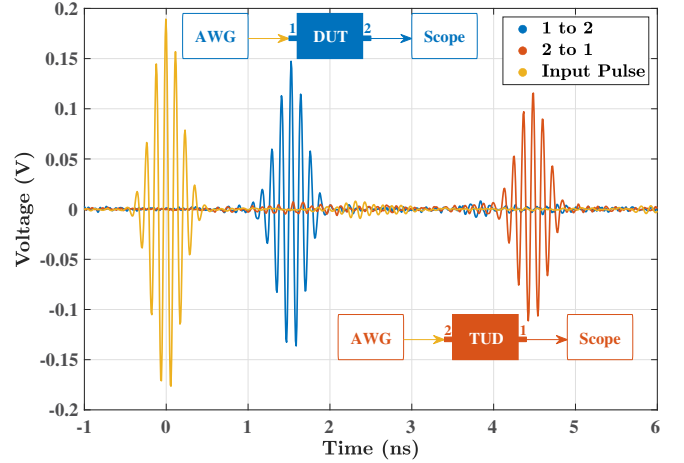

FIG. 7. Time-domain measurements for the microwave ring-graph (the DUT here) shown in Fig. 4(a). Insets show the schematic of the time-domain setup for the $1 \to 2$ and $2 \to 1$ measurements. The yellow pulse is a measurement of the incident pulse (a 1-ns wide Gaussian amplitude modulation of a $f_c = 8.5$ GHz carrier signal) from the arbitrary waveform generator (AWG) to the oscilloscope and establishes the baseline pulse amplitude. The blue pulse shows the transmitted pulse from port 1 to port 2, while the orange pulse shows the transmitted pulse from port 2 to port 1. Note that for the port 2 to port 1 measurement the DUT orientation is reversed.

frequency domain measurements of the same graph (green line). Figure 3(b) shows a plot of σ_V at a pulse center frequency of 8.5 GHz versus the lumped attenuation on each bond $\Gamma_A/2$, as they are varied together (red diamonds). Adjusting both attenuators to the same attenuation setting preserves identical electrical path lengths on the two bonds of the microwave graph [Fig. 4(b)]. We see once again the nonmonotonic dependence of transmission asymmetry on variable lumped attenuation, and good agreement between frequency domain $\langle P_{21} - P_{12} \rangle$ and time domain σ_V measurements.

V. DISCUSSION

We note some interesting parallels between the measurements on the classical microwave graph and earlier simulations of asymmetric transport in a model mesoscopic device with dephasing centers. The mesoscopic calculation in Fig. 3(d) shows a nonmonotonic dependence of asymmetric left/right transmission probability $P_{21} - P_{12}$ as a function of the average number of inelastic scattering events per passage based on a phenomenological model of the quantum mesoscopic system, illustrated in the inset [12,35]. Plotting the lumped attenuation Γ_A in units of Nepers (a $1/e$ decay of amplitude) is roughly analogous to the number of inelastic scattering events per passage of the wave packet through the device. A plot of asymmetric transmission versus $\Gamma_A/2$ from microwave data has essentially the same dependence as simulated transmission probability asymmetry plotted versus the average number of inelastic scattering events per passage, as shown in Fig. 8 (see also Fig. S6 in Supplemental Material [89] section "Detailed microwave AB-ring graph results"). The similarities are illustrated in
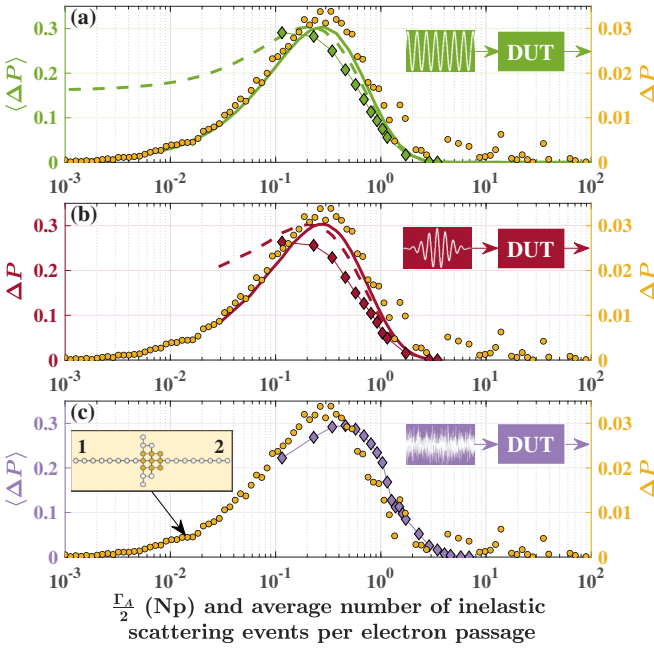
FIG. 8. Comparison of AB-graph microwave analogue asymmetric transmission (ΔP on left axis) and simulated mesoscopic device transmission probability asymmetry (ΔP on right axis), as a function of attenuation $\Gamma_A/2$ in Nepers, and average number of inelastic scattering events per electron passage, on a common log scale. Microwave measurements and simulation results are obtained in the (a) frequency-domain, (b) time-domain, and (c) frequency-resolved noise transmission. Lines and symbols have the same meaning as those in the corresponding parts of Fig. 3. The mesoscopic simulation results ΔP (in yellow) are the same in all panels [12,35].

Fig. 8 for (a) frequency-domain, (b) time-domain, and (c) broadband noise transmission. In the unitary evolution (zero attenuation) limit, there is symmetric transmission due to the purely coherent properties of the system. At large decoherence (attenuation) rates, the scattering events are so frequent that they destroy any bias for the electrons (microwaves) to follow a particular direction through the device, sometimes explained as a manifestation of the quantum Zeno effect [101]. Only in the intermediate decoherence (attenuation) case does the combination of coherent transport, along with a finite degree of modeled decoherence (attenuation) acting asymmetrically, result in a net transmission asymmetry through the device.

From the perspective of the PCP, this unique state is not observed in either the purely coherent or strongly attenuated limits, but is a unique feature of wave systems augmented by a finite number of parasitic lossy channels. Similar results on asymmetric transport of a Bose-Einstein condensate through an AB-ring analogue in cold atoms, as a function of loss rate (analogous the the attenuation used here), shows the same qualitative dependence as those in Figs. 3 and 8 [40]. It has also been proposed that transport of excitations across dissipative quantum networks can be enhanced by local dephasing noise, and the dependence of transport probability on dephasing rate is nonmonotonic [18,19]. Experiments on electronic excitation transport through a network of coupled trapped ions

shows evidence of environment-assisted quantum transport (ENAQT) effects that are also a nonmonotonic function of dephasing rate [21,22]. There are also proposals for dephasing assisted transport in coupled quantum dot systems [102,103].

There have also been classical wave transport experiments that demonstrate similar behavior to that shown in Figs. 3 and 8. A classical optics experiment involving noisy resonators on a fiber network demonstrated a peak in the dependence of the transport efficiency as a function of the amount of "dephasing noise" in the network, realizing the phenomenon of "noise-assisted transport" [104]. Another classical optics experiment utilizes variable input optical bandwidth to enhance transport [105].

It is remarkable that the measured microwave transmission asymmetry and the phenomenological mesoscopic dephasing treatment of asymmetric electron transport [12,35] have the same dependence on the loss/dephasing parameter over such a wide dynamic range. One possible reason for this is that the dephasing model effectively results in the same non-Hermitian treatment of the system Hamiltonian, and consequent modification of the scattering matrix, as observed for classical waves. This conclusion is consistent with all three observations discussed here, namely the experimental data on the classical wave analogue of the AB-graph, the simulated results for an asymmetric mesoscopic scatterer of Refs. [12,35], and the dissipative cold-atom experiment modeling an AB-graph in momentum space [40]. In fact, the nonmonotonic dependence of transmission probability on "dephasing" or measurement rates seems to be a generic property of many treatments of quantum transport, such as environment-assisted quantum transport [18,19,21] and monitored quantum devices [106,107]. This leaves open the question of whether a more detailed or microscopic treatment of dephasing in quantum systems might arrive at different conclusions with regards to asymmetric transmission.

The microwave ring-graph elegantly captures the fundamental wave interference, nonreciprocal and dissipative properties that give rise to asymmetric transmission. Of course, there are a number of limitations of the analogy between electromagnetic (EM) and mesoscopic quantum systems. In the EM analogue there are no Fermi-Dirac statistics, a linear (as opposed to quadratic) dispersion relation, and no electron-electron interactions. The physics of entanglement and superposition states are also absent in the classical case. In the EM case the microwave photons are dissipated, whereas in the mesoscopic case the particle number is conserved. Finally, the wave-packet time evolution is different in detail, owing to the first-order nature of the time-dependent Schrodinger equation versus the second-order nature of the EM wave equation. In addition the PCP approach to accounting for absorption in classical wave systems (or dephasing in quantum systems) is entirely phenomenological and generic in nature, detached from microscopic theory. For example, it fails to capture multiparticle quantum interactions that lead to dephasing.

Next we comment on several properties of the microwave graph. It is well established that nonreciprocal wave transport can be created by a simple microwave device known as an isolator. One might ask: how does the microwave analogue of the AB-ring graph differ from an isolator? An isolator can be
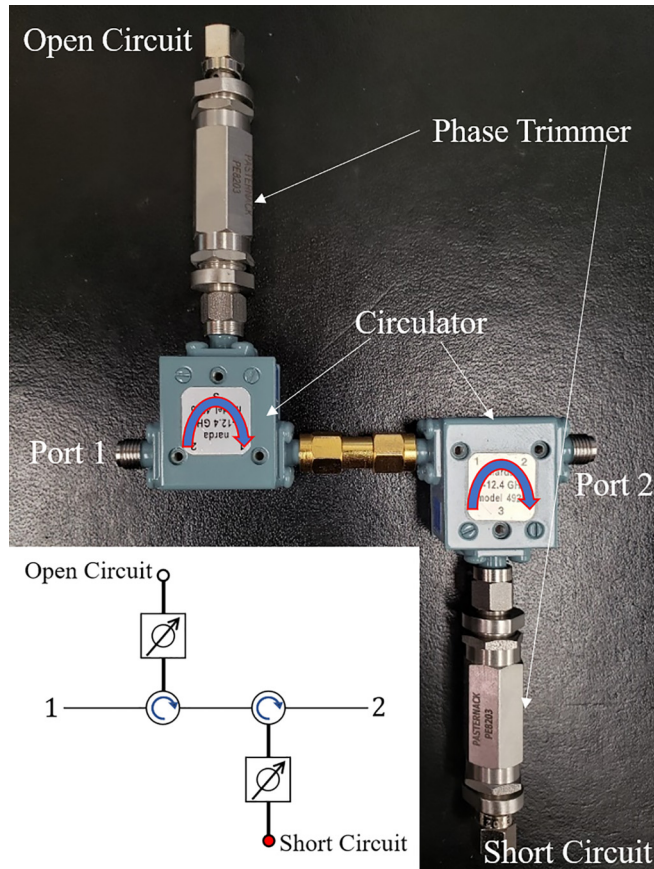
FIG. 9. The schematic design and photograph of a microwave gyrator offering nonreciprocal π phase difference between the left-going waves and right-going waves traveling between ports 1 and 2. Two nominally identical circulators are used to guide the wave propagation directions, and a pair of open/short circuits are used to create the π phase difference for waves traveling in different directions. Between the open/short circuits and the circulators, there are a pair of phase trimmers for calibrating the phase shift on the two vertical branches of the circuit.

fabricated from a three-terminal circulator, like those utilized in our design for the gyrator (see Fig. 9). The second port of the circulator is connected to a matched load that absorbs energy injected into port 1 and circulated to port 2. Waves entering port 3 are directed to port 1, creating a two-port device that passes waves in one direction while absorbing those going in the opposite direction. We note that photons absorbed and then re-emitted from the absorptive load will be forced to circulate to port 3, due to the design of the device. In contrast the microwave AB-ring graph has a crucial difference. Photons absorbed and re-emitted by the localized attenuators $\Gamma_A/2$ are able to exit the device through either port, with equal probability. This feature is utilized in the phenomenological mesoscopic analogue model to create the asymmetric flow of electrons in that case [12,35].

A second important feature of the microwave graph concerns its linearity. It is well established that nonreciprocal transport can be achieved by exploiting nonlinearities. A common example is the diode, which has a nonlinear current-voltage characteristics at large voltage amplitudes, but a linear

response at low amplitude [34]. In Fig. S5 of Ref. [89] we demonstrate that the asymmetric transmission of the microwave AB-graph is present over a broad range of amplitude excitation. Its ability to create asymmetric transmission is not based on nonlinear processes or features.

VI. CONCLUSIONS

In this paper, we present a two-port microwave network structure that demonstrates a 3:1 ratio of the transmission time delays for waves traveling in opposite directions. The 3:1 ratio of the time delay has been illustrated in both frequency-domain and time-domain experiments. Using both simulations and experiments, we also demonstrate the asymmetric transmission through the microwave ring in both the frequency domain and time domain. The degree of asymmetric transmission is shown to be a nonmonotonic function of localized attenuation in the ring. The experimental results on asymmetric transmission exist for both coherent and incoherent signal sources. We find that a particular phenomenological model of decoherence in mesoscopic quantum systems produces a very similar dependence of transmission asymmetry on dephasing rate.

APPENDIX A: CST SIMULATIONS

Figure S1 of Ref. [89] shows the simulation schematic of the microwave ring-graph as a CST circuit model. Each port leads to a three-way tee junction that acts as a beam-splitter and combiner for the incident waves from either direction, but having finite reflection for waves arriving on all three transmission lines. The upper branch is a finite length of uniform coaxial cable transmission line, while the lower branch contains a model gyrator. The upper and lower branches are chosen to have the same electrical length to eliminate Feshbach resonances of the ring [95,99] and both branches contain a lumped-loss variable attenuator. The model closely approximates the experimental realization of the AB-analogue microwave graph. The model allows introduction of lumped loss Γ_A (variable attenuator) and uniform loss η (in all the coaxial cables) to the graph. Using Eq. S1 in Ref. [89], the value of η can be shown to range from 0.00741 to 0.00767 GHz in the frequency band 8.25–8.75 GHz used in Figs. 3 and 8.

The shape modes of the ring graph involve standing wave patterns around the circumference of the ring and having a large overlap with propagating modes on the two leads [95,99,108]. The resulting poles and zeros of the scattering matrix are located relatively far from the real-frequency axis [95,99]. The Feshbach modes are an orthogonal set of modes

that have minimal overlap with the extended modes on the leads, and create poles and zeros near the real-frequency axis [95,99], giving rise to narrow spectral features.

APPENDIX B: AHARONOV-BOHM-ANALOGUE MICROWAVE GRAPH

Figure 9 shows the schematic design and photograph of the microwave gyrator setup. A wave traveling from port 1 to port 2 will be directed upwards and reflect from the open circuit on the left circulator, while the wave traveling in the opposite direction from port 2 will be directed downwards and reflect from the short circuit on the right circulator. The open/short circuits are designed to provide a π phase difference for waves traveling in opposite directions, but due to the unequal finite electrical length of the components inside the circuits, the phase difference is not exactly π. Thus, we add a pair of carefully adjusted phase trimmers in the design to compensate for the difference in electrical lengths. (This basic idea of creating 0 and π phase shifts for left- and right-going waves was inspired by the graph presented in Ref. [109].)

The measured phase difference between S_{12} and S_{21} between ports 1 and 2 in Fig. 9 as a function of frequency is shown in Fig. S3 of Ref. [89]. The circulators used in the experiment have a working frequency range of 7–12.4 GHz, and we measure the S-matrix of the gyrator in that frequency range. This broad frequency range enables the time-domain measurements with wave packets. After doing some fine-tuning of the two phase trimmers, we are able to get the phase difference from the gyrator to be close to π across the frequency band. We also verify that the insertion loss of the gyrator is symmetric (Fig. S3(b) of Ref. [89]). There are some small wiggles in these plots, which are due to the imperfection of the circulators and resulting standing waves inside the circuit. Note that the circulators contain microwave ferrites that are biased by a dc magnetic field in a fixed direction, dictating the circulation direction. The operating bandwidth of the circulators is what limits the overall bandwidth of the entire microwave ring-graph. Further characterization of the gyrator is given in Supplemental Material [89] section "Gyrator Properties."

Figure 4(b) shows a photograph of the assembled microwave AB-ring graph with two identical attenuators present. Further characterization of this circuit is given in Supplemental Material [89] section "Detailed microwave ring-graph results."

APPENDIX C: COMPLEX TIME DELAY

We have introduced a generalized version of time delay applicable to non-Hermitian (in this case subunitary) scattering systems, such as the ring graph with either uniform or lumped attenuation, or both. The Wigner-Smith time delay for an M-port scattering system described by the $M \times M$ scattering matrix S measured as a function of frequency f is defined as [91] $\tau_W \equiv \frac{-i}{M} \frac{d}{df} \log \det S(f)$. This definition is a straightforward generalization of the Wigner-Smith time delay, previously considered only in the context of unitary quantum systems, to include variations in the magnitude of the scattering matrix with frequency. The complex Wigner-Smith time delay as a function of frequency can be expressed in terms of the pole and zero locations of the scattering matrix S [76,91] (see Supplemental Material [89] section "Poles and Zeros of the S-Matrix of the Microwave Ring-Graph"). We also utilize the complex reflection and transmission time delays to identify the zeros of the reflection and transmission submatrices, respectively. In this paper we evaluate the asymmetric complex transmission time delays of the $M = 2$-port microwave ring-graph as [95] $\tau_T^{12} \equiv -i \frac{d}{df} \log[S_{12}(f)]$ and $\tau_T^{21} \equiv -i \frac{d}{df} \log[S_{21}(f)]$. We have previously utilized all of the complex time delays to characterize the shape and Feshbach modes of the ordinary (as opposed to AB-like) ring graph in terms of the zeros and poles of the scattering matrix and its transmission and reflection submatrices [95].

Please see the Supplemental Material [89] and the additional references [110–117] therein for additional details for the simulations and experiments.

[1] C. Jarzynski, Equalities and inequalities: Irreversibility and the second law of thermodynamics at the nanoscale, Annu. Rev. Condens. Matter Phys. **2**, 329 (2011).

[2] U. Seifert, Stochastic thermodynamics, fluctuation theorems and molecular machines, Rep. Prog. Phys. **75**, 126001 (2012).

[3] W. H. Zurek, Decoherence and the transition from quantum to classical, Phys. Today **44**, 36 (1991).

[4] J. F. Poyatos, J. I. Cirac, and P. Zoller, Quantum reservoir engineering with laser cooled trapped ions, Phys. Rev. Lett. **77**, 4728 (1996).

[5] E. Joos, *Decoherence and the Appearance of a Classical World in Quantum Theory*, 2nd ed. (Springer, Berlin, 2003).

[6] W. H. Zurek, Decoherence, einselection, and the quantum origins of the classical, Rev. Mod. Phys. **75**, 715 (2003).

[7] S. Fortin and O. Lombardi, The correspondence principle and the understanding of decoherence, Found. Phys. **49**, 1372 (2019).

[8] D. Braak and J. Mannhart, Fermi's golden rule and the second law of thermodynamics, Found. Phys. **50**, 1509 (2020).

[9] J. Wang, G. Benenti, G. Casati, and W.-G. Wang, Quantum chaos and the correspondence principle, Phys. Rev. E **103**, L030201 (2021).

[10] H.-P. Breuer and F. Petruccione, *The Theory of Open Quantum Systems* (Oxford University Press, Oxford, UK, 2002).

[11] R. D. Astumian and P. Hänggi, Brownian motors, Phys. Today **55**, 33 (2002).

[12] J. Mannhart, H. Boschker, and P. Bredol, Non-unitary quantum electronics: Novel functions from the edge of the quantum world, Nano Express **2**, 014008 (2021).

[13] B. Kraus, H. P. Büchler, S. Diehl, A. Kantian, A. Micheli, and P. Zoller, Preparation of entangled states by quantum Markov processes, Phys. Rev. A **78**, 042307 (2008).

[14] F. Verstraete, M. M. Wolf, and J. Ignacio Cirac, Quantum computation and quantum-state engineering driven by dissipation, Nat. Phys. **5**, 633 (2009).

[15] J. T. Barreiro, M. Müller, P. Schindler, D. Nigg, T. Monz, M. Chwalla, M. Hennrich, C. F. Roos, P. Zoller, and R. Blatt, An open-system quantum simulator with trapped ions, Nature (London) **470**, 486 (2011).

[16] M. Müller, S. Diehl, G. Pupillo, and P. Zoller, Engineered open systems and quantum simulations with atoms and ions, in *Advances In Atomic, Molecular, and Optical Physics*, edited by P. Berman, E. Arimondo, and C. Lin (Academic Press, San Diego, CA, 2012), Vol. 61, pp. 1–80.

[17] G. García-Pérez, M. A. C. Rossi, and S. Maniscalco, IBM Q experience as a versatile experimental testbed for simulating open quantum systems, npj Quantum Inf. **6**, 1 (2020).

[18] M. B. Plenio and S. F. Huelga, Dephasing-assisted transport: Quantum networks and biomolecules, New J. Phys. **10**, 113019 (2008).

[19] P. Rebentrost, M. Mohseni, I. Kassal, S. Lloyd, and A. Aspuru-Guzik, Environment-assisted quantum transport, New J. Phys. **11**, 033003 (2009).

[20] F. Caruso, A. W. Chin, A. Datta, S. F. Huelga, and M. B. Plenio, Highly efficient energy excitation transfer in light-harvesting complexes: The fundamental role of noise-assisted transport, J. Chem. Phys. **131**, 105106 (2009).

[21] C. Maier, T. Brydges, P. Jurcevic, N. Trautmann, C. Hempel, B. P. Lanyon, P. Hauke, R. Blatt, and C. F. Roos, Environment-assisted quantum transport in a 10-qubit network, Phys. Rev. Lett. **122**, 050501 (2019).

[22] E. Zerah-Harush and Y. Dubi, Effects of disorder and interactions in environment assisted quantum transport, Phys. Rev. Res. **2**, 023294 (2020).

[23] S. O. Valenzuela, W. D. Oliver, D. M. Berns, K. K. Berggren, L. S. Levitov, and T. P. Orlando, Microwave-induced cooling of a superconducting qubit, Science **314**, 1589 (2006).

[24] A. Cabot, F. Carollo, and I. Lesanovsky, Continuous sensing and parameter estimation with the boundary time crystal, Phys. Rev. Lett. **132**, 050801 (2024).

[25] J. C. Maxwell, *Theory of Heat* (Longmans, Green, and Co., New York, NY, 1872).

[26] V. Čápek and D. Sheehan, *Challenges to The Second Law of Thermodynamics* (Springer, Dordrecht, 2005).

[27] P. Reimann, Brownian motors: Noisy transport far from equilibrium, Phys. Rep. **361**, 57 (2002).

[28] Y. Tokura and N. Nagaosa, Nonreciprocal responses from non-centrosymmetric quantum materials, Nat. Commun. **9**, 3740 (2018).

[29] L. Zhu and S. Fan, Near-complete violation of detailed balance in thermal radiation, Phys. Rev. B **90**, 220301(R) (2014).

[30] L. Zhu and S. Fan, Persistent directional current at equilibrium in nonreciprocal many-body near field electromagnetic heat transfer, Phys. Rev. Lett. **117**, 134303 (2016).

[31] S. Lepri and G. Casati, Asymmetric wave propagation in nonlinear systems, Phys. Rev. Lett. **106**, 164101 (2011).

[32] N. Bender, S. Factor, J. D. Bodyfelt, H. Ramezani, D. N. Christodoulides, F. M. Ellis, and T. Kottos, Observation of asymmetric transport in structures with active nonlinearities, Phys. Rev. Lett. **110**, 234101 (2013).

[33] J. Mannhart, Non-reciprocal interferometers for matter waves, J. Supercond. Novel Magn. **31**, 1649 (2018).

[34] P. Bredol, Nonreciprocity of the wave-packet scattering delay in ballistic two-terminal devices, Phys. Rev. B **103**, 035404 (2021).

[35] P. Bredol, H. Boschker, D. Braak, and J. Mannhart, Decoherence effects break reciprocity in matter transport, Phys. Rev. B **104**, 115413 (2021).

[36] Y. Aharonov and D. Bohm, Significance of electromagnetic potentials in the quantum theory, Phys. Rev. **115**, 485 (1959).

[37] J. Mannhart and D. Braak, Lossless currents at high temperatures, J. Supercond. Novel Magn. **32**, 17 (2019).

[38] J. Mannhart, Beyond superconductivity, J. Supercond. Novel Magn. **33**, 249 (2020).

[39] O. Entin-Wohlman, Y. Imry, A. G. Aronov, and Y. Levinson, Orbital magnetization in the hopping regime, Phys. Rev. B **51**, 11584 (1995).

[40] W. Gou, T. Chen, D. Xie, T. Xiao, T.-S. Deng, B. Gadway, W. Yi, and B. Yan, Tunable nonreciprocal quantum transport through a dissipative Aharonov-Bohm ring in ultracold atoms, Phys. Rev. Lett. **124**, 070402 (2020).

[41] H.-J. Stöckmann, *Quantum Chaos: An Introduction* (Cambridge University Press, Cambridge, UK, 1999).

[42] H. J. Stöckmann, Why do an experiment, if theory is exact, and any experiment can at best approximate theory? Phys. Scr. **2001**, 246 (2001).

[43] S. W. McDonald and A. N. Kaufman, Spectrum and eigenfunctions for a Hamiltonian with stochastic trajectories, Phys. Rev. Lett. **42**, 1189 (1979).

[44] H. J. Stockmann and J. Stein, Quantum chaos in billiards studied by microwave-absorption, Phys. Rev. Lett. **64**, 2215 (1990).

[45] E. Doron, U. Smilansky, and A. Frenkel, Experimental demonstration of chaotic scattering of microwaves, Phys. Rev. Lett. **65**, 3072 (1990).

[46] S. Sridhar and E. J. Heller, Physical and numerical experiments on the wave mechanics of classically chaotic systems, Phys. Rev. A **46**, R1728 (1992).

[47] A. Kudrolli, V. Kidambi, and S. Sridhar, Experimental studies of chaos and localization in quantum wave functions, Phys. Rev. Lett. **75**, 822 (1995).

[48] A. Richter, Wave dynamical chaos: An experimental approach in billiards, Phys. Scr. **T90**, 212 (2001).

[49] Y.-H. Kim, M. Barth, H.-J. Stöckmann, and J. P. Bird, Wave function scarring in open quantum dots: A microwave-billiard analog study, Phys. Rev. B **65**, 165317 (2002).

[50] Y. H. Kim, M. Barth, U. Kuhl, H.-J. Stöckmann, and J. P. Bird, Scanning fourier spectroscopy: A microwave analog study to image transmission paths in quantum dots, Phys. Rev. B **68**, 045315 (2003).

[51] D. Dragoman and M. Dragoman, *Quantum-Classical Analogies*, The Frontiers collection, 1612-3018 (Springer, Berlin, 2004).

[52] Y. H. Kim, U. Kuhl, H. J. Stockmann, and J. P. Bird, Investigating dynamical tunnelling in open quantum dots by means of a soft-walled microwave-cavity analogue, J. Phys.: Condens. Matter **17**, L191 (2005).

[53] P. Seba, U. Kuhl, M. Barth, and H. J. Stockmann, Experimental verification of topologically induced vortices inside a billiard, J. Phys. A: Math. Gen. **32**, 8225 (1999).

[54] L. Pauling, The diamagnetic anisotropy of aromatic molecules, J. Chem. Phys. **4**, 673 (1936).

[55] O. Hul, S. Bauch, P. Pakoński, N. Savytskyy, K. Życzkowski, and L. Sirko, Experimental simulation of quantum graphs by microwave networks, Phys. Rev. E **69**, 056205 (2004).

[56] D. Agassi, H. A. Weidenmüller, and G. Mantzouranis, The statistical theory of nuclear reactions for strongly overlapping resonances as a theory of transport phenomena, Phys. Rep. **22**, 145 (1975).

[57] J. Verbaarschot, H. Weidenmüller, and M. Zirnbauer, Grassmann integration in stochastic quantum physics: The case of compound-nucleus scattering, Phys. Rep. **129**, 367 (1985).

[58] H. A. Weidenmüller, Stochastic scattering theory random-matrix models for fluctuations in microscopic and mesoscopic systems, in *Chaos and Quantum Chaos*, edited by W. D. Heiss (Springer, Berlin, 2005), pp. 121–166.

[59] Y. V. Fyodorov and H.-J. Sommers, Statistics of resonance poles, phase shifts and time delays in quantum chaotic scattering: Random matrix approach for systems with broken time-reversal invariance, J. Math. Phys. **38**, 1918 (1997).

[60] Y. V. Fyodorov, D. V. Savin, and H.-J. Sommers, Scattering, reflection and impedance of waves in chaotic and disordered systems with absorption, J. Phys. A: Math. Gen. **38**, 10731 (2005).

[61] G. E. Mitchell, A. Richter, and H. A. Weidenmüller, Random matrices and chaos in nuclear physics: Nuclear reactions, Rev. Mod. Phys. **82**, 2845 (2010).

[62] Y. V. Fyodorov and D. V. Savin, Resonance scattering of waves in chaotic systems, in *The Oxford Handbook of Random Matrix Theory*, edited by G. Akemann, J. Baik, and P. D. Francesco (Oxford University Press, Oxford, UK, 2011), pp. 703–722.

[63] U. Kuhl, O. Legrand, and F. Mortessagne, Microwave experiments using open chaotic cavities in the realm of the effective Hamiltonian formalism, Fortschr. Phys. **61**, 404 (2013).

[64] H. Schomerus, Random matrix approaches to open quantum systems, in *Stochastic Processes and Random Matrices: Lecture Notes of the Les Houches Summer School 2015*, edited by G. Schehr, A. Altland, Y. V. Fyodorov, N. O'Connell, and L. F. Cugliandolo (Oxford University Press, Oxford, UK, 2017), pp. 409–473.

[65] M. Osman and Y. V. Fyodorov, Chaotic scattering with localized losses: *S*-matrix zeros and reflection time difference for systems with broken time-reversal invariance, Phys. Rev. E **102**, 012202 (2020).

[66] Y. V. Fyodorov and D. V. Savin, Statistics of impedance, local density of states, and reflection in quantum chaotic systems with absorption, J. Exp. Theor. Phys. Lett. **80**, 725 (2004).

[67] S. Hemmady, X. Zheng, E. Ott, T. M. Antonsen, and S. M. Anlage, Universal impedance fluctuations in wave chaotic systems, Phys. Rev. Lett. **94**, 014102 (2005).

[68] O. Hul, O. Tymoshchuk, S. Bauch, P. M. Koch, and L. Sirko, Experimental investigation of Wigner's reaction matrix for irregular graphs with absorption, J. Phys. A: Math. Gen. **38**, 10489 (2005).

[69] X. Zheng, T. Antonsen, and E. Ott, Statistics of impedance and scattering matrices in chaotic microwave cavities: Single channel case, Electromagnetics **26**, 3 (2006).

[70] X. Zheng, T. M. Antonsen, and E. Ott, Statistics of impedance and scattering matrices of chaotic microwave cavities with multiple ports, Electromagnetics **26**, 37 (2006).

[71] G. Akguc and L. E. Reichl, Effect of evanescent modes and chaos on deterministic scattering in electron waveguides, Phys. Rev. E **64**, 056221 (2001).

[72] S. Hemmady, J. Hart, X. Zheng, T. M. Antonsen, E. Ott, and S. M. Anlage, Experimental test of universal conductance fluctuations by means of wave-chaotic microwave cavities, Phys. Rev. B **74**, 195326 (2006).

[73] M. Büttiker, Role of quantum coherence in series resistors, Phys. Rev. B **33**, 3020 (1986).

[74] P. W. Brouwer and C. W. J. Beenakker, Voltage-probe and imaginary-potential models for dephasing in a chaotic quantum dot, Phys. Rev. B **55**, 4695 (1997).

[75] C. Benjamin and A. M. Jayannavar, Dephasing via stochastic absorption: A case study in Aharonov-Bohm oscillations, Phys. Rev. B **65**, 153309 (2002).

[76] L. Chen, S. M. Anlage, and Y. V. Fyodorov, Statistics of complex Wigner time delays as a counter of *S*-matrix poles: Theory and experiment, Phys. Rev. Lett. **127**, 204101 (2021).

[77] T. Kottos and U. Smilansky, Quantum chaos on graphs, Phys. Rev. Lett. **79**, 4794 (1997).

[78] T. Kottos and U. Smilansky, Periodic orbit theory and spectral statistics for quantum graphs, Ann. Phys. **274**, 76 (1999).

[79] M. J. Richardson and N. L. Balazs, On the network model of molecules and solids, Ann. Phys. **73**, 308 (1972).

[80] P. Exner, Lattice Kronig-Penney Models, Phys. Rev. Lett. **74**, 3503 (1995).

[81] J. A. Sánchez-Gil, V. Freilikher, I. Yurkevich, and A. A. Maradudin, Coexistence of ballistic transport, diffusion, and localization in surface disordered waveguides, Phys. Rev. Lett. **80**, 948 (1998).

[82] J. T. Chalker and P. D. Coddington, Percolation, quantum tunnelling and the integer Hall effect, J. Phys. C **21**, 2665 (1988).

[83] D. Kowal, U. Sivan, O. Entin-Wohlman, and Y. Imry, Transmission through multiply-connected wire systems, Phys. Rev. B **42**, 9009 (1990).

[84] W. Hu, J. C. Pillay, K. Wu, M. Pasek, P. P. Shum, and Y. D. Chong, Measurement of a topological edge invariant in a microwave network, Phys. Rev. X **5**, 011012 (2015).

[85] B. Dietz, V. Yunko, M. Białous, S. Bauch, M. Ławniczak, and L. Sirko, Nonuniversality in the spectral properties of time-reversal-invariant microwave networks and quantum graphs, Phys. Rev. E **95**, 052202 (2017).

[86] T. Ghutishvili, L. Chen, S. M. Anlage, and T. M. Antonsen, Impedance statistics of cable networks that model quantum graphs, Phys. Rev. Res. **5**, 033195 (2023).

[87] J. W. Strutt, V. On the constant of magnetic rotation of light in bisulphide of carbon, Philos. Trans. R. Soc. London **176**, 343 (1885).

[88] Rayleigh, On the magnetic rotation of light and the second law of thermo-dynamics, Nature (London) **64**, 577 (1901).

[89] See Supplemental Material at http://link.aps.org/supplemental/10.1103/PhysRevB.110.045103 for additional details for the simulations and experiments (gyrator properties, pulse transmission details, linearity of asymmetric transmission, comparisons of asymmetric transmission between data, and quantum simulation). Also included are measurements of the poles and zeros of the scattering matrix of the AB-ring graph, simulation and experimental results for an AB-ring graph with an attenu-

ator on just one of the bonds, and some brief comments about dephasing models.

[90] M. Asano, K. Y. Bliokh, Y. P. Bliokh, A. G. Kofman, R. Ikuta, T. Yamamoto, Y. S. Kivshar, L. Yang, N. Imoto, Ş. K. Özdemir, and F. Nori, Anomalous time delays and quantum weak measurements in optical micro-resonators, Nat. Commun. **7**, 13488 (2016).

[91] L. Chen, S. M. Anlage, and Y. V. Fyodorov, Generalization of Wigner time delay to subunitary scattering systems, Phys. Rev. E **103**, L050203 (2021).

[92] P. del Hougne, K. B. Yeo, P. Besnier, and M. Davy, On-demand coherent perfect absorption in complex scattering systems: Time delay divergence and enhanced sensitivity to perturbations, Laser Photon. Rev. **15**, 2000471 (2021).

[93] Y. Kang and A. Z. Genack, Transmission zeros with topological symmetry in complex systems, Phys. Rev. B **103**, L100201 (2021).

[94] Y. Huang, Y. Kang, and A. Z. Genack, Wave excitation and dynamics in non-Hermitian disordered systems, Phys. Rev. Res. **4**, 013102 (2022).

[95] L. Chen and S. M. Anlage, Use of transmission and reflection complex time delays to reveal scattering matrix poles and zeros: Example of the ring graph, Phys. Rev. E **105**, 054210 (2022).

[96] B. D. Tellegen, The gyrator: A new electric network element, Philips Res. Rep. **3**, 81 (1948).

[97] C. L. Hogan, The ferromagnetic faraday effect at microwave frequencies and its applications, Rev. Mod. Phys. **25**, 253 (1953).

[98] G. Viola and D. P. DiVincenzo, Hall effect gyrators and circulators, Phys. Rev. X **4**, 021019 (2014).

[99] D. Waltner and U. Smilansky, Scattering from a ring graph—A simple model for the study of resonances, Acta Phys. Pol. A **124**, 1087 (2013).

[100] M. Białous, P. Dulian, A. Sawicki, and L. Sirko, Delay-time distribution in the scattering of short Gaussian pulses in microwave networks, Phys. Rev. E **104**, 024223 (2021).

[101] B. Misra and E. C. G. Sudarshan, The Zeno's paradox in quantum theory, J. Math. Phys. **18**, 756 (1977).

[102] L. D. Contreras-Pulido, M. Bruderer, S. F. Huelga, and M. B. Plenio, Dephasing-assisted transport in linear triple quantum dots, New J. Phys. **16**, 113061 (2014).

[103] L. P. Bettmann, M. J. Kewming, and J. Goold, Thermodynamics of a continuously monitored double-quantum-dot heat engine in the repeated interactions framework, Phys. Rev. E **107**, 044102 (2023).

[104] S. Viciani, M. Lima, M. Bellini, and F. Caruso, Observation of noise-assisted transport in an all-optical cavity-based network, Phys. Rev. Lett. **115**, 083601 (2015).

[105] D. N. Biggerstaff, R. Heilmann, A. A. Zecevik, M. Gräfe, M. A. Broome, A. Fedrizzi, S. Nolte, A. Szameit, A. G. White, and I. Kassal, Enhancing coherent transport in a photonic network using controllable decoherence, Nat. Commun. **7**, 11282 (2016).

[106] B. Annby-Andersson, F. Bakhshinezhad, D. Bhattacharyya, G. De Sousa, C. Jarzynski, P. Samuelsson, and P. P. Potts, Quantum Fokker-Planck master equation for continuous feedback control, Phys. Rev. Lett. **129**, 050401 (2022).

[107] J. Ferreira, T. Jin, J. Mannhart, T. Giamarchi, and M. Filippone, Transport and nonreciprocity in monitored quantum devices: An exact study, Phys. Rev. Lett. **132**, 136301 (2024).

[108] P. Exner and J. Lipovský, Resonances from perturbations of quantum graphs with rationally related edges, J. Phys. A: Math. Theor. **43**, 105301 (2010).

[109] A. Rehemanjiang, M. Allgaier, C. H. Joyner, S. Müller, M. Sieber, U. Kuhl, and H.-J. Stöckmann, Microwave realization of the Gaussian symplectic ensemble, Phys. Rev. Lett. **117**, 064101 (2016).

[110] J. Erb, D. Shrekenhamer, T. Sleasman, T. M. Antonsen, and S. M. Anlage, Control of the scattering properties of complex systems by means of tunable metasurfaces, Acta Phys. Pol. A **144**, 421 (2023).

[111] J. Mannhart, P. Bredol, and D. Braak, Phase filters for a novel kind of asymmetric transport–scientific prospects and opportunities for possible applications, Physica E **109**, 198 (2019).

[112] Y. Ohashi and T. Momoi, On the bloch theorem concerning spontaneous electric current, J. Phys. Soc. Jpn. **65**, 3254 (1996).

[113] R. Leturcq, D. Sánchez, G. Götz, T. Ihn, K. Ensslin, D. C. Driscoll, and A. C. Gossard, Magnetic field symmetry and phase rigidity of the nonlinear conductance in a ring, Phys. Rev. Lett. **96**, 126801 (2006).

[114] B. Szafran, B. Rzeszotarski, and A. Mreńca-Kolasińska, Topologically protected wave packets and quantum rings in silicene, Phys. Rev. B **100**, 085306 (2019).

[115] T. Novotný, Investigation of apparent violation of the second law of thermodynamics in quantum transport studies, Europhys. Lett. **59**, 648 (2002).

[116] A. Levy and R. Kosloff, The local approach to quantum transport may violate the second law of thermodynamics, Europhys. Lett. **107**, 20004 (2014).

[117] H. Fröml, A. Chiocchetta, C. Kollath, and S. Diehl, Fluctuation-induced quantum Zeno effect, Phys. Rev. Lett. **122**, 040402 (2019).